Selective Rubidium Recovery Using Zeolitic Potassium Hexacyanoferrate Nanomaterial Electrode in Capacitive Deionization

Dai Quyet Truong, Youngwoo Choo, Tien Vinh Nguyen, and Gayathri Naidu*

Rubidium (Rb) mining from seawater brine is promising as a sustainable renewable resource. Selectively recovering Rb from saline brine is challenging. Capacitive deionization (CDI), an electrosorption process, offers the capacity to extract Rb rapidly with selective electrodes. This study reports CDI electrodes utilizing potassium cobalt hexacyanoferrate (KCoFC-AC) and ZIF-embedded KCoFC (KCoFC@ZIF-AC) nanomaterials for selective Rb uptake. The feasibility of the fabricated Rb-selective electrodes is established by detail electrochemical characterizations. Compared to conventional carbon electrode, the fabricated electrodes exhibited a notably higher Rb selectivity. Specifically, the Rb uptake capacities of the composite electrodes with single Rb and mixed monovalent solution (Rb, Na, K) ranged from 78 to 127 mg g^{-1} and 57 to 103 mg g^{-1}, respectively. The enhanced performance of KCoFC@ZIF-AC compared to KCoFC-AC is attributed to the presence of the ZIF component, which promotes Rb penetration into the lattice structure of KCoFC. Moreover, the saturated electrodes demonstrated reusability multiple times with periodic chemical regeneration processes. In seawater, both fabricated electrodes exhibited an excellent Rb extraction rate ($\approx$90%) with minor uptake of major cations (Na, Mg, K, and Ca). The superior Rb selectivity of the fabricated electrodes underscore the role of ion-exchange nanomaterial in CDI electrode for achieving rapid Rb extraction from brine.

1. Introduction

Rubidium (Rb) is an economically valuable metal with a high market price estimated at $27 825 kg^{-1} in 2022.[1] The high price of Rb is due to the rarity of mining and separating Rb in land ores.[2] Rb is an essential ingredient for the defence and medical industry, specifically used to develop high-precision lasers for submarines' precise targeting from underwater, atomic clocks

D. Q. Truong, Y. Choo, T. V. Nguyen, G. Naidu
School of Civil and Environmental Engineering
University of Technology Sydney (UTS)
City Campus, Broadway, NSW 2007, Australia
E-mail: Gayathri.Danasamy@uts.edu.au

The ORCID identification number(s) for the author(s) of this article can be found under https://doi.org/10.1002/sstr.202500273.

as quantum global positioning system navigators for ships and navy vessels, and medical CT scan beams.[3–5] Natural water sources such as salt lakes and seawater brine are considered promising alternative and renewable resources of Rb supply.[1,6,7]

Our team developed a selective ion exchange nanomaterial, potassium cobalt hexacyanoferrate (KCoFC),[8–11] exhibiting high selective Rb uptake in seawater. In our recent work, Truong et al.[12] established the modification of KCoFC with the zeolitic imidazole framework (ZIF) nanoparticles, resulting in up to eight times higher Rb uptake capacity than the pristine KCoFC. Nevertheless, this material has several drawbacks that restrict its application for Rb recovery in aqueous brine solutions. Firstly, this material is in powder form, which limits its direct application in an ion exchange column. Moreover, it requires a substantial amount of time to reach equilibrium (at least 8–12 h).[9,10,12] In addition, chemical regeneration is required to release and extract Rb from the nanomaterial, which invariably requires further separation steps to attain purified Rb salts.[8]

In this regard, electrochemical capacitive deionization (CDI) offers the possibility of achieving rapid uptake of ions that can be released via reverse charge, thereby avoiding chemical regeneration and further separation. Briefly, CDI is a deionization process that is predominantly driven by the electrosorption mechanism. The CDI module consists of an electrode pair, and each piece could play a role as an anode or cathode, according to the electrical polarity applied. In the presence of an electrical potential lower than the water splitting potential ($\leq$1.23 V), within a short operational period (typically within 20 min), cations and anions in a solution would be electrosorbed into the electric double layer (EDL) formed at the surfaces of the cathode and anode, respectively. Upon equilibrium, the reverse voltage or short-circuit method is applied to expel the ions from the saturated electrodes.[13] Thereafter, the electrodes are regenerated and reused for the subsequent cycle. Generally, the CDI electrodes are synthesized from highly porous carbon-based materials, primarily activated carbon (AC), to maximize the specific charge density.[14] However, AC exhibits poor selectivity toward targeted ions in the complex solution and seawater.[15,16]

Embedding and incorporating selective nanomaterials onto AC electrodes provides highly selective features to the CDI

**ADVANCED
SCIENCE NEWS**

www.advancedsciencenews.com

**small
structures**

www.small-structures.com

process. Several studies have developed specific fabricated CDI electrodes for practical and economic element recovery purposes.[17–22] For example, Shang et al.[23] introduced a highly lithium-selective material named $LiNi_{0.5}Mn_{1.5}O_4$ to act as the cathode with an AC negative electrode in a hybrid cell. The electrode was reported to achieve the Li sorption capacity of $260\,\mu mol\,g^{-1}$, which was three times higher compared with the conventional AC cell, and simultaneously maintained the high selectivity toward Li in aqueous solution with the presence of high Mg concentration ($C_{Mg}/C_{Li} = 30$). Similarly, Roobavannan et al.[24] fabricated Li selective electrodes from zeolitic imidazolate framework encapsulated manganese oxide nanomaterials.[25] The fabricated electrode achieved a high Li selectivity over other cations ($\rho_{Na}^{Li} = 13.14$, $\rho_K^{Li} = 6.60$, $\rho_{Mg}^{Li} = 1.69$). In another study, Wang et al.[26] reported on a high-efficiency CuSe electrode to selectively remove and recover copper from an electroplating effluent through a hybrid CDI platform. Lee et al.[27] utilized copper hexacyanoferrate (CuHCF) material to develop a novel electrode for removing Cs from liquid radioactive waste. The fabricated electrode had an excellent Cs uptake capacity of $397\,mg\,g^{-1}$ and excellent selectivity in cation mixtures. Given the high Rb selectivity exhibited by KCoFC ion exchange nanomaterial, as established by our previous work,[8–10,12] KCoFC is envisioned to be a promising material for fabricating a highly selective CDI electrode for Rb separation from an aqueous solution.

From the authors' knowledge, an investigation on selective Rb extraction with CDI in an aqueous solution has not been carried out. Therefore, this study aims to develop novel electrodes for Rb capture from seawater by utilizing potassium cobalt hexacyanoferrate (KCoFC) and ZIF-grafted KCoFC (KCoFC@ZIF) nanomaterials. The fabricated electrodes were well-established by combining KCoFC/KCoFC@ZIF and AC with polyvinylidene fluoride (PVDF) as a binder. Cyclic voltammetry (CV), galvanostatic charge–discharge (GCD), and temperature-dependent electrochemical impedance spectroscopy (EIS) analyses were implemented to evaluate the electrochemical properties of the fabricated electrodes. The adsorption and desorption processes were conducted consecutively under the voltage of ±1.2 V

with Rb single solution and deionized water, respectively. Furthermore, the selectivity for Rb compared with other competition cations in mixed monovalent solutions and seawater solutions (raw and Rb-spiked samples) was investigated for multiple operational cycles. Eventually, the potential to regenerate saturated electrodes after numerous operational series (each series consists of five absorption/desorption cycles) was also evaluated.

2. Results and Discussion

2.1. Characterization of Electrodes

Figure 1a–d demonstrates the scanning electron microscopy (SEM) images of the AC electrode along with three other composite electrodes, ZIF-AC, KCoFC-AC, and KCoFC@ZIF-AC. As depicted in Figure 1a, the pristine AC electrode exhibits irregularly shaped porous carbon chunks with a broad size distribution ranging from 1 to 10 μm. In contrast, the ZIF-AC electrode clearly displays leaf-like ZIF crystals, sized between 2 and 3 μm, covering the surface of the AC electrode and creating a hierarchical structure (Figure 1b). Figure 1c reveals the KCoFC-AC electrode's surface, characterized by a mixture of carbon blocks and smaller KCoFC nanoparticles, resulting in a highly porous multiscale structure. Eventually, the KCoFC@ZIF-AC electrode, illustrated in Figure 1d, exhibits its KCoFC granules whose surfaces are well-encapsulated by bright, submicron-sized particles, representing a layer of ZIF crystals.

The energy dispersive X-ray spectroscopy (EDS) spectra of the representative electrodes, KCoFC-AC and KCoFC@ZIF-AC, further clarify the composition of the fabricated electrodes, as shown in Figure S2, Supporting Information. Both electrodes demonstrate high C content (>50%), reflecting the carbon-rich nature of the electrode material. The presence of potassium (K) was confirmed, with mass percentages of 5.47% and 0.77% for KCoFC-AC and KCoFC@ZIF-AC electrodes, respectively, underscoring the incorporation of ion-exchangeable K within the composite electrodes. Additionally, a zinc (Zn) signal is observed at a
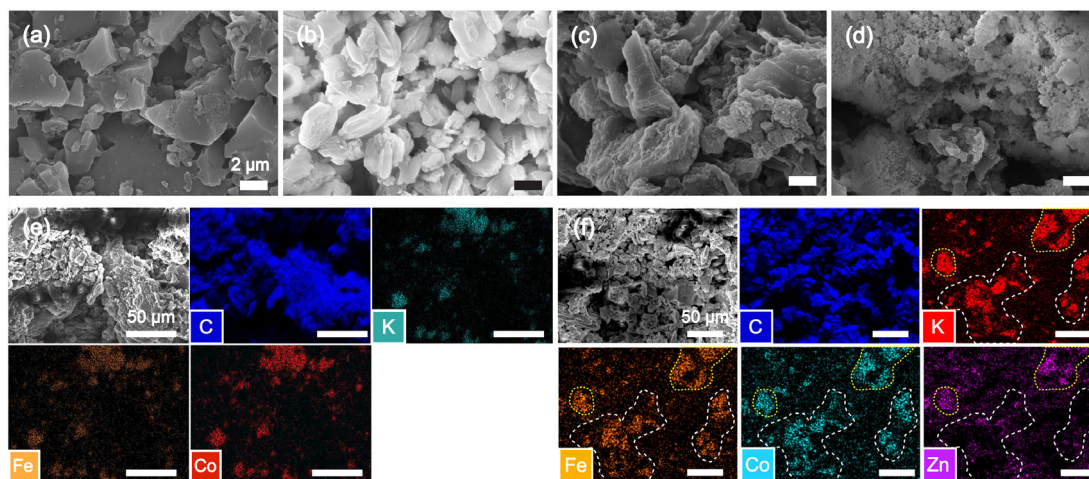

Figure 1. SEM images of a) AC, b) ZIF-AC, c) KCoFC-AC, and d) KCoFC@ZIF-AC electrodes. EDS images of e) KCoFC-AC and f) KCoFC@ZIF-AC electrodes.

ADVANCED
SCIENCE NEWS
www.advancedsciencenews.com

small
structures
www.small-structures.com

mass percentage of 2.6% in the KCoFC@ZIF-AC electrode, indirectly indicating the successful integration of ZIF crystals onto the surface of the KCoFC particles. The EDS elemental maps of the fabricated electrodes reveal the distribution of elements across the electrode surfaces (Figure 1(e–f)). The images display a dominating carbon signal across the surface, attributable to the AC underlying layer. Additionally, the presence of K, Fe, and Co in overlapping areas, forming globular structures, suggests that the KCoFC particles are uniformly distributed and well-adhered to the AC electrode surface (Figure 1e). Figure 1f further confirms the colocalization of K, Fe, and Co, indicating the successful formation of KCoFC particles. Notably, a Zn signal is also detected in these regions (highlighted by yellow dotted areas), strongly suggesting that the ZIF particles have effectively coated the KCoFC particles. An area rich in KCoFC with a comparatively weaker Zn signal (highlighted by white dashed lines) was also identified. We presume that the areal density of the ZIF crystals covering these specific areas is lower than other sections of the KCoFC@ZIF composites, implying that ZIF crystals are more

sparsely attached to the KCoFC@ZIF composite particles in these areas.

Powder X-ray diffraction (XRD) results are presented in **Figure 2**a. The XRD measurements were conducted on the powder sample before mixing it with AC particles because AC exhibits intense diffraction peaks around 20°–30°, which overlap with the second reflection peak of KCoFC. The XRD pattern for KCoFC@ZIF reveals strong peaks at 17.5°, 24.8°, and 35.4°, corresponding to the [2 0 0], [2 2 0], [4 0 0] crystal planes of KCoFC, respectively. A notable observation is the slight shift of these peaks toward lower angles and their broadening in the KCoFC@ZIF sample compared to neat KCoFC. This peak shift suggests the possibility of Zn ion intercalation into the KCoFC crystalline structure, leading to an increase in lattice parameters and inducing a partial disorder of the lattice structure. In addition, the peaks corresponding to the ZIF crystals appear weaker than those of the KCoFC crystals in the XRD data. This is likely due to the disproportionate volume fractions of the two materials. As evidenced by the EDS mapping, the ZIF-L crystals are
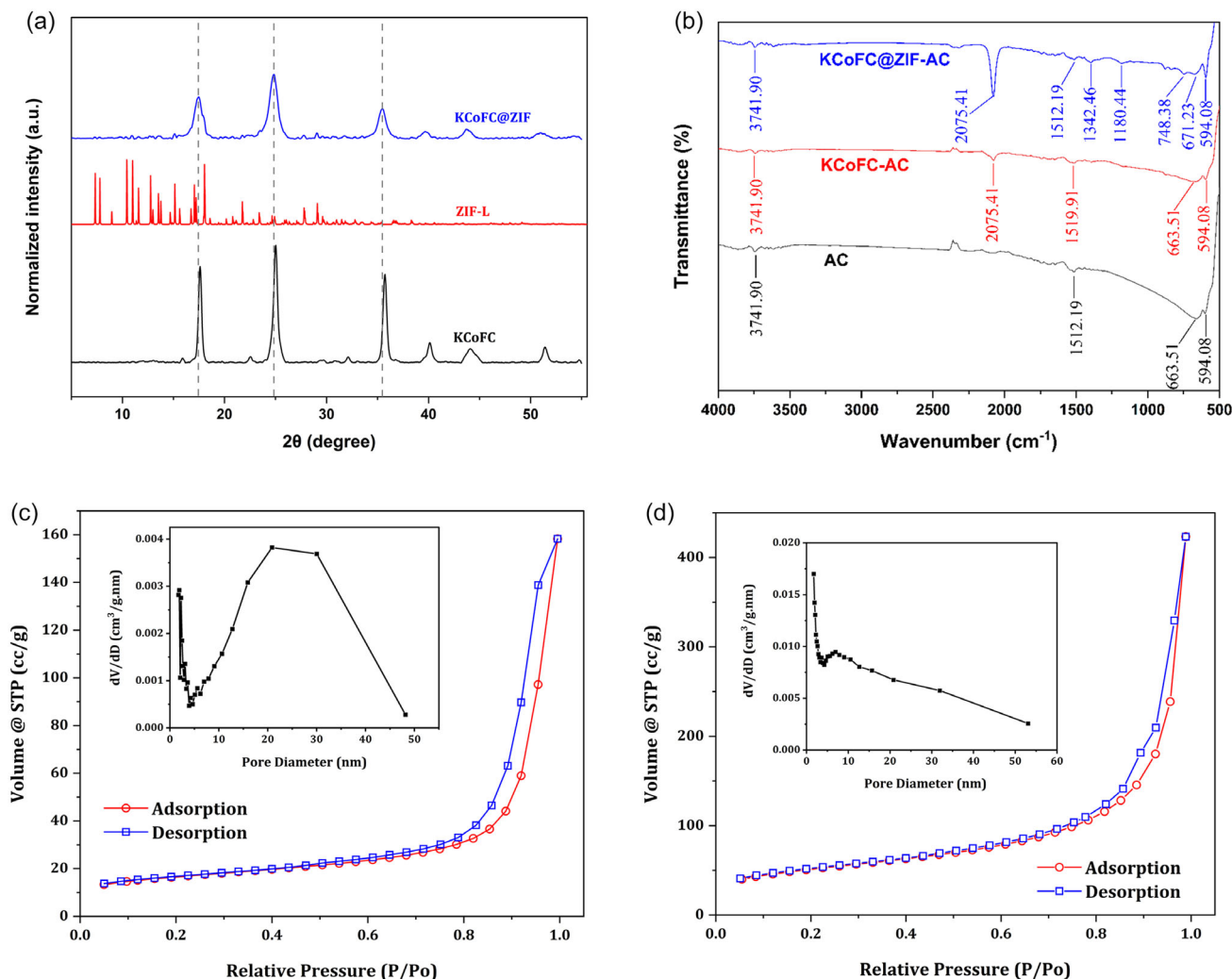

Figure 2. a) Powder XRD patterns of the neat KCoFC, ZIF-L, and KCoFC@ZIF particles; b) FTIR pattern of AC, KCoFC-AC, and KCoFC@ZIF-AC electrodes; N$_2$ adsorption–desorption isotherms and pore size distributions of c) KCoFC and d) KCoFC@ZIF nanomaterials.

**ADVANCED
SCIENCE NEWS**

www.advancedsciencenews.com

**small
structures**

www.small-structures.com

present in areas colocalized with KCoFC, while their areal density is significantly lower than that of KCoFC. This discrepancy in volume ratio likely results in the observed reduction in peak intensities of ZIF-L in the KCoFC@ZIF composite.

Figure 2b depicts the fourier-transform infrared spectroscopy (FTIR) spectra of the activated carbon electrode alongside the KCoFC and KCoFC@ZIF composite electrodes. The significant volume fraction of the activated carbon component within these composite electrodes results in the observation of typical peaks across the spectra. In particular, a weak peak at $3741.90\,cm^{-1}$ is attributed to the stretching vibration of the hydroxyl group (—OH),[28] and a peak at $1512.19\,cm^{-1}$ is assignable to the C=C stretch in aromatic rings.[29] Additionally, the absorption band at $663.51\,cm^{-1}$ corresponds to the alkyne group C≡C.[30] However, the sharp absorption peaks observed at 2075.41 and $593\,cm^{-1}$ in both modified electrodes are linked to the stretching vibrations of the cyano groups (C≡N)[31] and Fe–CN–Co complex,[32] respectively, indicating the presence of the KCoFC particles. Meanwhile, the KCoFC@ZIF-AC spectrum exhibits the absorption bands at 1342.46 and $748.38\,cm^{-1}$, reflecting the bending vibrations of the C—N single bond and the C=N double bond, respectively.[33,34] These specific absorption bands were attributed to the imidazole group present in ZIF crystals, thus verifying the successful integration of the composite nanomaterial, KCoFC@ZIF, with activated carbon.

Figure 2c,d show the N_2 adsorption–desorption isotherms and pore size distribution diagram. The Brunauer–Emmett–Teller surface area, pore volume, and mean pore diameter for KCoFC and KCoFC@ZIF are summarized in Table S3, Supporting Information. Integrating the ZIF component into the KCoFC particles notably improves the structural characteristics of the porous material, enhancing both surface area and pore size. Specifically, the specific surface area increased from $55.74\,m^2\,g^{-1}$ for the neat KCoFC to $177.15\,m^2\,g^{-1}$ for KCoFC@ZIF, marking an enhancement of more than threefold. Similarly, the pore volume of the ZIF-modified KCoFC nanomaterial was nearly triple that of the unmodified KCoFC, increasing from 0.24 to $0.65\,cm^3\,g^{-1}$. This increase can be attributed to the introduction of the smaller pores of ZIF nanocrystals.[12] Consequently, the mean pore diameter for KCoFC@ZIF was reduced to 17.92 nm, compared to 24.45 nm for the original KCoFC sorbent.

2.2. Electrochemical Characterization

Figure S4, Supporting Information, demonstrates the cyclic voltammogram of the commercial activated carbon and fabricated KCoFC-AC/KCoFC@ZIF-AC electrodes at a scan rate ranging from 5 to $100\,mV\,s^{-1}$ in 0.1 M RbCl solution. The CV curves of those electrodes exhibit a typical leaf-like shape with no apparent oxidation/reduction peak, suggesting an ideal EDL formation without any Faradaic reaction occurring over the entire potential range. The specific capacitances at different scan rates are presented in Figure S4d, Supporting Information. It is noticed that the specific capacitance values decreased gradually with scan rates as expected. A low scan rate allows sufficient time for the ion transport from the bulk solution to the electrolyte-electrode interface, thus favoring the sorption process.[35] As

the scan speed increases, the ion transport is limited, reducing the EDL capacity.[36] Furthermore, it is evident that the specific capacitance (C) of the AC commercial electrode was notably higher than that of the other fabricated electrodes at each scan rate, which is attributed to a relatively lower electric conductivity of KCoFC/KCoFC@ZIF nanomaterials compared to the conductive AC material. Specifically, the specific capacitance of KCoFC@ZIF-AC was similar to that of the KCoFC-AC electrode, suggesting an equivalent EDL electrosorption capacity between the two synthesized nanomaterials.

Regarding the GCD measurement, Figure S5, Supporting Information, presents the GC curves of AC commercial and fabricated electrodes at a current density of $0.1\,A\,g^{-1}$ and a potential window ranging from −0.2 to 0.6 V. Apparently, the well-maintained triangular shape can be observed in all electrodes, indicating the adequate electrochemical stability and reversibility of these electrodes.[36,37] Furthermore, a longer discharging time (≈425 s) was observed in the AC commercial electrode (Figure S5a, Supporting Information) compared to those in other electrodes (≈65–75 s), suggesting a higher electrosorption capacity of the neat AC electrode. In addition, the potential drop of the AC electrode ($iR = 0.05$ V) is significantly smaller than that of KCoFC-AC/KCoFC@ZIF-AC electrodes ($iR = 0.15$ V), indicating the lower inner resistance of the commercial electrode compared to the fabricated electrodes.

EIS measurements were performed in the frequency range of 100 kHz to 0.2 Hz with an amplitude of 10 mV over a temperature range of 25–45 °C to determine the activation energy (E_a) of the Rb^+ electrosorption process at the electrode–electrolyte interface. As depicted in Figure S6a–c, Supporting Information, all three electrodes (i.e., AC commercial, KCoFC-AC, and KCoFC@ZIF-AC) presented similar Nyquist plots, characterized by a quasi-semicircle in the high-frequency region and a straight line in the low-frequency region. Notably, the charge transfer resistance (R_{ct}, Ω) was estimated from the x-intercept and the diameter of the semicircles. The activation energy, E_a, was then calculated using the Arrhenius equation.[38,39] Table S4, Supporting Information, presents the R_{ct} values of each electrode at different temperatures. It is evident that the magnitude of R_{ct} increases with temperature, which is contrary to previous observations reported in the literature.[40,41] This anomalous behavior is likely due to enhanced Rb^+ desorption at elevated temperatures, which is unfavorable for the electrosorption in the CDI systems.[42,43] As a result, the calculated E_a values were negative for all three electrodes (Table S4, Supporting Information), suggesting that the electrosorption process is largely dominated by thermal fluctuation. Despite the negative E_a values, the magnitudes of E_a still provide insight into ion-electrode interaction. Electrodes with smaller absolute E_a values are considered to have stronger ion–surface interactions and are less prone to thermally induced desorption, thereby maintaining higher ion uptake. According to Table S4, Supporting Information, the $|E_a|$ of KCoFC-AC ($E_a = -13.43\,kJ\,mol^{-1}$) and KCoFC@ZIF-AC ($E_a = -17.41\,kJ\,mol^{-1}$) are relatively smaller than that of the AC electrode ($E_a = -20.27\,kJ\,mol^{-1}$), indicating more stable performance and lower energy barriers for Rb^+ ion transport from the electrolyte into the solid phase.

The series of electrochemical characterizations implies that the incorporation of highly selective Rb sorption nanomaterials

(i.e., KCoFC/KCoFC@ZIF) compromised the charge conductivity of the electrodes. Therefore, adding the conductive AC alongside selective KCoFC/KCoFC@ZIF nanomaterials is essential to compensate for the conductivity. Further electrosorption experiments are carried out and presented in the following sections to comprehensively investigate the capacitive ion storage capability of the synthesized electrodes.

2.3. Rb-Ion Transportation and Selectivity of the Fabricated KCoFC-AC and KCoFC@ZIF-AC Electrodes

The Rb uptake in an Rb-only solution with CDI incorporated with AC, KCoFC-AC, and KCoFC@ZIF-AC electrodes exhibited a similar performance range between 50-57% (**Figure 3**a). KCoFC@ZIF-AC achieved a slightly higher Rb uptake by 2–5% compared to AC and KCoFC@AC electrodes. The ZIF-AC electrode showed a rate of around 50% Rb uptake, which was closely similar to that of the AC electrode (51%), suggesting that the ZIF material did not have a unique role in Rb uptake.

Conversely, in the mixed monovalent solution, both AC and ZIF-AC electrodes demonstrate a notably lower Rb uptake than the Rb single solution (Figure 3a). Specifically, Rb uptake was reduced to around 9–12% in a mixed solution for both AC and ZIF-AC electrodes. On the contrary, in a mixed solution, the performance of KCoFC-AC and KCoFC@ZIF-AC declined marginally to that of the Rb-only solution, achieving 46–47% Rb uptake. It is essential to highlight that although both KCoFC-AC and KCoFC@ZIF-AC achieved a similar Rb uptake range, in terms of performance capacity (based on the mass of ion exchange material), the KCoFC@ZIF-AC electrode achieved a substantially higher Rb uptake at $103.17\,\mathrm{mg\,g^{-1}}$ than that of KCoFC-AC at $56.39\,\mathrm{mg\,g^{-1}}$ (Figure 3b). As mentioned in the Introduction section, CDI has not yet been explored for Rb extraction. Consequently, a direct performance comparison with existing CDI studies is not feasible. Nonetheless, several studies have investigated the fabrication of selective electrodes for Rb recovery using electrochemical methods.[44–47] For instance, Zhang et al.[45] fabricated the copper hexacyanoferrate $(Cu_3[Fe(CN)_6]_2)$ electrode and utilized K^+ as the shuttle ion. By conducting multiple electrochemical steps, including K^+ intercalation, Rb^+ electrosorption, and Rb^+ deintercalation, Rb ion species could be directly extracted from the simulated salt lake solution. In addition, the separation coefficients between Rb^+ and K^+, Ca^{2+}, Na^+, and Mg^{2+} were reported at 63, 585, 1635, and 2543, respectively. Likewise, Wang et al.[47] employed a typical 2×4 tunnel manganese oxide material named Octahedral molecular sieve-5 (OMS-5) for the preparation of a
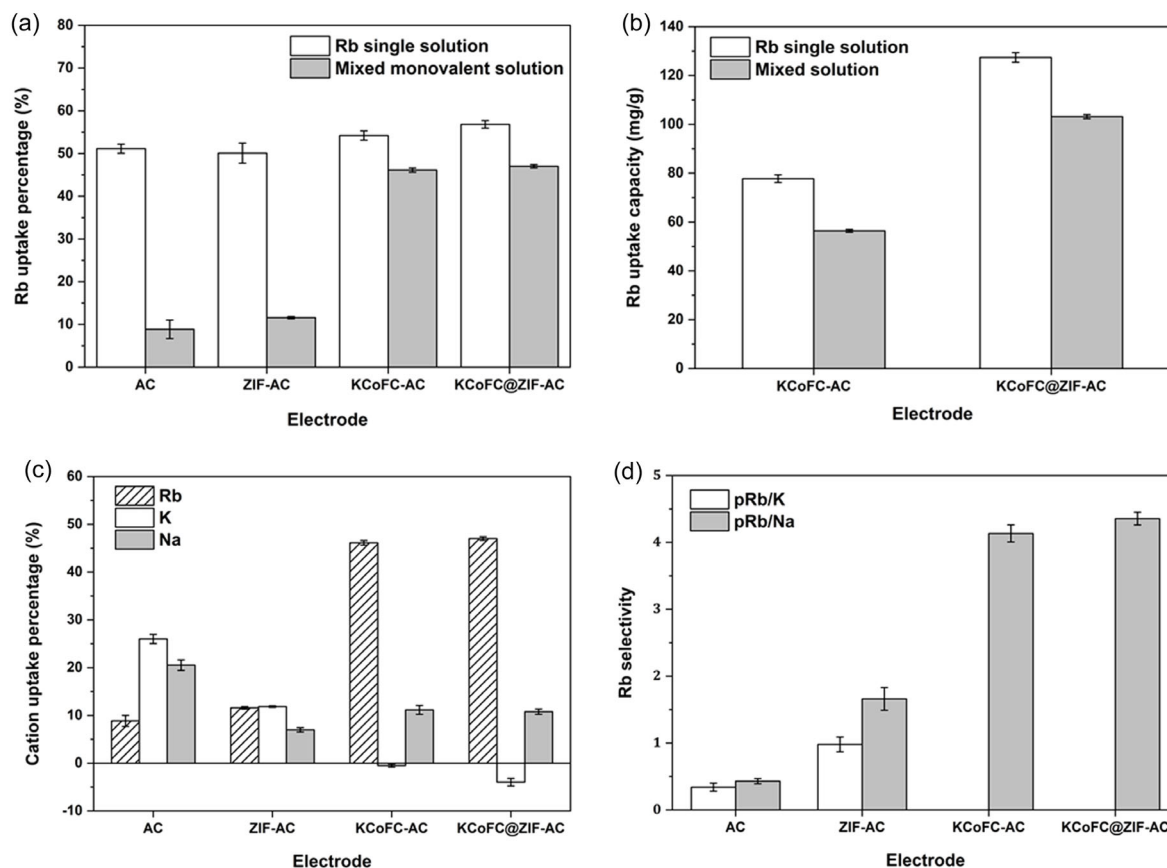

Figure 3. Comparison between the fabricated electrodes in terms of a) Rb uptake percentage (%) in Rb single solution and mixed monovalent solution; b) Rb uptake capacity ($\mathrm{mg\,g^{-1}}$); c) cation uptake percentage (%) in the mixed monovalent solution, and d) Rb relative selectivity toward K (ρ_K^{Rb}) and Na (ρ_{Na}^{Rb}).

novel faradaic electrode (H-OMS-5) with the purpose of Rb$^+$ enrichment in aqueous solution. Due to a synergistic mechanism between the ion exchange and the supercapacitor ion storage process, the fabricated H-OMS-5 electrode exhibited remarkable Rb$^+$ sorption capacity ($Q_{max} = 390.3$ mg g^{-1}). However, the protonation of OMS-5 pristine material to obtain H-OMS-5 required extensive chemical consumption (1 M HMO$_3$) over an extended period (1 day), which impedes the manganese oxide-derived electrode from being widely applied in real-world scenarios.

With regards to selectivity, the AC electrode showed a 12–17% higher uptake for Na and K over Rb (Figure 3c). As a result, the relative Rb selectivity toward Na ($\rho_{Na}^{Rb} = 0.34$) and K ($\rho_K^{Rb} = 0.43$) was less than 1 (Figure 3d). The poor Rb selectivity over Na and K by the AC electrode does not follow the conventional principle of electrosorption. Specifically, within a group of similarly charged ions, the smaller the hydrated ionic diameter, the higher the electrosorption capacity onto the carbonaceous material.[48] The monovalent hydrated ionic diameter follows the order of Rb (6.58 Å) < K (6.62 Å) < Na (7.16 Å) (Table S5, Supporting Information). As such, it is expected that the AC electrode should demonstrate a preference for Rb over Na and K; nevertheless, this was not the case. In a previous study,[49] monovalent cations with lower hydration enthalpy were indicated to show a more favorable affinity for electro-sorption in an AC electrode-based CDI setting. According to Table S5, Supporting Information, compared to Na ($\Delta H = 406$ KJ mol^{-1}) and K ($\Delta H = 322$ KJ mol^{-1}), Rb exhibits a relatively lower hydration enthalpy of 293 KJ mol^{-1}. Theoretically, the AC electrode may show a higher cation uptake selectivity toward Rb than other monovalent cations (i.e., Na and K). However, the contrary result displaying lower Rb uptake with AC electrode could be associated with ionic charge efficiency, by which ion with a high charge density would exhibit higher electrosorption affinity[50] Compared to Rb ($C_d = 8.35$ C mm^{-3}), the higher charge density parameter of Na ($C_d = 23.24$ C mm^{-3}) and K ($C_d = 11.09$ C mm^{-3}) could be relevant to the improvement of the Coulombic attraction between these cations and the carbonaceous material; thus, the AC electrode selectivity followed the order of K > Na > Rb attained a better uptake selectivity toward K and Na over Rb ionic species. This suggests that the conventional AC electrode is not applicable for selective rubidium extraction from the mixed ionic solution.

Compared to the AC electrode, the ZIF-AC electrode followed a different electrosorption pattern in the order of Rb ≥ K > Na. This order was in line with the smallest hydrated ionic diameter of Rb (6.58 Å), showing higher uptake over K (6.62 Å) and Na (7.16 Å). This scenario indicates that it is likely that the narrow pore size of ZIF enabled to fine-tune and control electrosorption based on element size. Consequently, ZIF-AC facilitated sieving and reducing Na and K uptake. Secondly, this could be related to the more hydrophobic nature of ZIF that repels ions with a higher ionic radius, which results in a relatively higher Rb selectivity. Specifically, the ρ_{Na}^{Rb} and ρ_K^{Rb} values were 1.66 and 0.98, respectively. Overall, it can be highlighted that ZIF plays a role in controlling ion electrosorption based on hydrated ionic size, which is an advantage in reducing Na and K uptake over Rb.

Contrary to the AC and ZIF-AC electrodes, both the fabricated electrodes exhibited minor sorption for Na (12% for the KCoFC-AC

electrode and 11% for the KCoFC@ZIF-AC electrode) (Figure 3c). Correspondingly, the high selectivity of Rb to Na was achieved by KCoFC-AC ($\rho_{Na}^{Rb} = 3.80$) and KCoFC@ZIF-AC ($\rho_{Na}^{Rb} = 4.36$), respectively. Meanwhile, the K concentration increased in the effluent over the initial solution with both KCoFC-AC and KCoFC@ZIF-AC electrodes (Figure 3c). This is highly likely due to the liberation of K over time from KCoFC particles during the process of Rb uptake, as discussed in our previous study.[9,10] Particularly, under the direct current application, the Rb-charged species in the bulk phase penetrated the EDL that formed between the solution and porous electrode, then replaced by the exchangeable K ions in the lattice of KCoFC particle.[12] These results establish that the ion exchange mechanism between K and Rb governs the transport of Rb ions for both modified electrodes. As a result, these electrodes achieved a relatively high Rb selectivity, which is well-matched with the observation in our prior study.[12]

In general, the KCoFC@ZIF-AC electrode achieved higher Rb extraction capacity than the KCoFC-AC electrode. Also, a higher quantity of K was released from KCoFC@ZIF-AC, even though the electrode contained a lower mass of the ion exchange material. This suggests that perhaps KCoFC@ZIF-AC provided more vacant sites for Rb uptake by releasing more K ions. This could be likely due to the presence of ZIF, which fine-tunes the pore size to match that of small Rb. To highlight the role of ZIF and KCoFC in enhancing Rb uptake, a more detailed investigation is carried out in the subsequent section.

2.4. Role of KCoFC Ion Exchange Material and ZIF Metal-Organic Frameworks Toward Selective Rb Uptake

In order to evaluate the role of KCoFC and ZIF MOFs in enhancing Rb uptake, several different electrode configurations were fabricated. KCoFC with ZIF was compared with KCoFC with Zn (denoted as KCoFC@Zn-AC) and KCoFC with HMIM (denoted as KCoFC@HMIM-AC). The electrosorption experiments with the mixed monovalent solution were also carried out using these new electrodes.

Figure 4 presents the performance comparison of these electrodes in terms of cation electrosorption efficiency and Rb relative selectivity in the mixed monovalent solution. The highly selective Rb efficiency of the fabricated electrodes derived from KCoFC nanomaterial relative to the AC electrode highlights the function of the KCoFC granule. Specifically, in the fabricated electrode layer, two ion capture mechanisms coexist: the physical sorption, or the electrostatic attraction by the applied direct current, and the chemical sorption by the selective material.[51–53] The physical sorption creates a weak and nonselective attraction between the ions in the bulk phase and the EDL in the electrode. The physical sorption represents the AC electrode that, in essence, displays weak selective Rb uptake. On the other hand, the chemical sorption (i.e., the ion exchange mechanism between the exchangeable function group in the material, in this case, K, and the specific cations in the feed solution generates a strong bonding to immobilize the specific Rb ions during the electrosorption process. Hence, the addition of a highly selective ion exchange nanomaterial (i.e., KCoFC) into the conventional
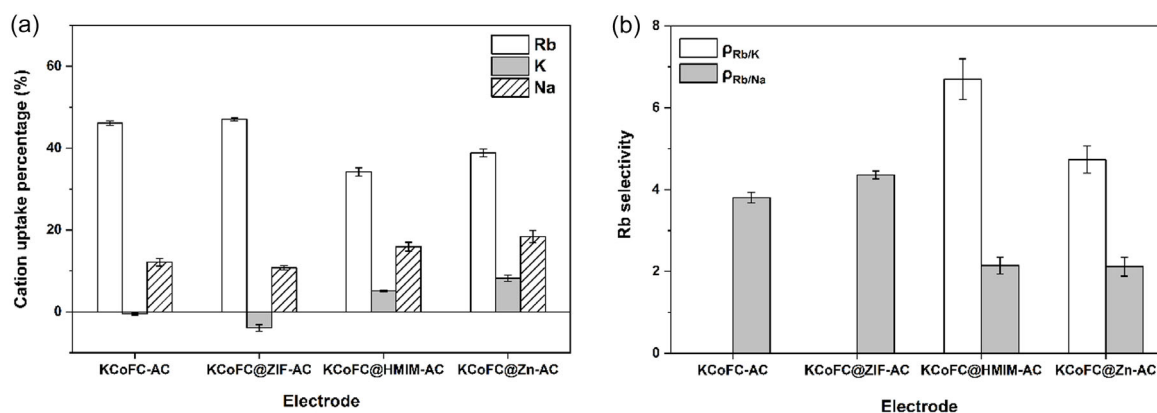
ADVANCED
SCIENCE NEWS

www.advancedsciencenews.com

small
structures

www.small-structures.com

Figure 4. a) Comparison between the KCoFC-based fabricated electrodes in terms of cation uptake percentage (%) in mixed monovalent solution and b) Rb relative selectivity compared to K (ρ_K^{Rb}) and Na (ρ_{Na}^{Rb}) of these electrodes (Due to the minus value of the K uptake percentage (%) by the KCoFC-AC and KCoFC@ZIF-AC electrode, the Rb relative selectivity compared to K (ρ_K^{Rb}) of these electrodes is not presented).

activated carbon electrode configuration significantly enhances the favorability of the electrode toward Rb in the CDI study.

The ion exchange between K and Rb in KCoFC/KCoFC@ZIF electrodes was established based on the high K released from the material as Rb was adsorbed from the mixed solution. In addition, it should be noted that due to the minus value of the K uptake percentage (%) by the KCoFC-AC and KCoFC@ZIF-AC electrodes, the Rb relative selectivity compared to K (ρ_K^{Rb}) was not determined mathematically and presented in Figure 4b.

Conversely, encapsulating the ZIF layer around the KCoFC particles favored the Rb penetration. Our previous study clarified that the MOF nanomaterial catalyzes the dehydration of the Rb-H_2O clusters when they enter the ZIF cavity; thus, the partially hydrated Rb ions could diffuse smoothly into the KCoFC inner lattice.[12] A density functional theory calculation as well as an in situ spectroscopy study corroborate that the dehydration of ions and further ion transport are promoted when the ion cluster is introduced into a confined geometry.[54–56] Furthermore, according to the performance of ZIF-AC and KCoFC@ZIF-AC electrodes compared to the conventional AC electrode (Figure 3a,c), it is likely that the ZIF layer created a specific ion diffusion pathway that fits with the Rb ionic size; thus formatting a barrier that selectively accepts Rb ion penetration into the core KCoFC particle. On the contrary, the infiltration of other monovalent ions (i.e., Na and K) into the intraparticle nanostructure of the KCoFC@ZIF was rejected; therefore, the Rb uptake selectivity was enhanced. In addition, according to the N_2 adsorption–desorption isotherms data (Table S3, Supporting Information), the surface area of the KCoFC@ZIF ion exchange material (177.15 $m^2 g^{-1}$) was enlarged by approximately three times compared to the pristine KCoFC material (55.74 $m^2 g^{-1}$), which may have contributed to the enhancement of the overall electrosorption capacity. Similarly, Roobavannan et al.[25] observed that the ZIF layer encapsulated onto the surface of hydrogen manganese oxide (HMO) material enlarged the surface area of the initial nanomaterial by ≈44 times (from 17.1 to 751.2 $m^2 g^{-1}$). Furthermore, the ZIF component provided some additional functional groups, along with the insertion of Zn ions into the lattice of HMO material, which also supported the deprotonation on the material's surface. Thus, in that study,

Li extraction capacity and selectivity were enriched, along with the acceleration of the sorption kinetics.

To understand the specific role of ZIF encapsulation onto KCoFC, two further combinations of electrodes were fabricated: KCoFC with Zn metal cluster as well as KCoFC with 2-methylimidazole organic linkers (HMIM), which are the two main ingredients of ZIF. Both KCoFC@HMIM and KCoFC@Zn electrodes underperformed in terms of Rb uptake and selectivity compared to KCoFC@ZIF and neat KCoFC electrodes (Figure 4a). These results suggest that grafting the Zn metal cluster and HMIM as individual materials onto KCoFC does not play a role in enhancing the Rb uptake. On the contrary, adding these materials onto KCoFC may have reduced vacant sites for K-Rb exchange, resulting in slightly reduced Rb uptake efficiency. On the other hand, the combination of these two materials, forming a ZIF structure, serves as a functional material with KCoFC. In this combination, ZIF characteristics, namely high specific surface area and crystalline structure, high porosity, and fine-tuned pore size, play a significant role in enhancing vacant sites for K-Rb exchange of KCoFC. This, in turn, enhanced Rb selectivity over Na in aqueous solution.

2.5. Desorption Performance

Following the electrosorption step, the desorption phase was carried out to recover the cations and regenerate the saturated electrodes. The desorption percentages of Rb and other species were calculated based on the amount of ions captured in the adsorption stage and discharged in the desorption progress.

2.5.1. Rb Desorption with AC and ZIF-AC Electrodes

Both AC and ZIF-AC electrodes achieved an extremely high Rb recovery efficiency (≥95%) in both solutions (**Figure 5**a,b). In the mixed solution experiment, the separation rate of Na and K followed a similar trend to that of Rb, which was ≈96–98%. The high desorption of all ions could be attributed to the ion capture mechanism, in which the electrosorption of the carbon-based electrode is based on the physical sorption by the electrostatic
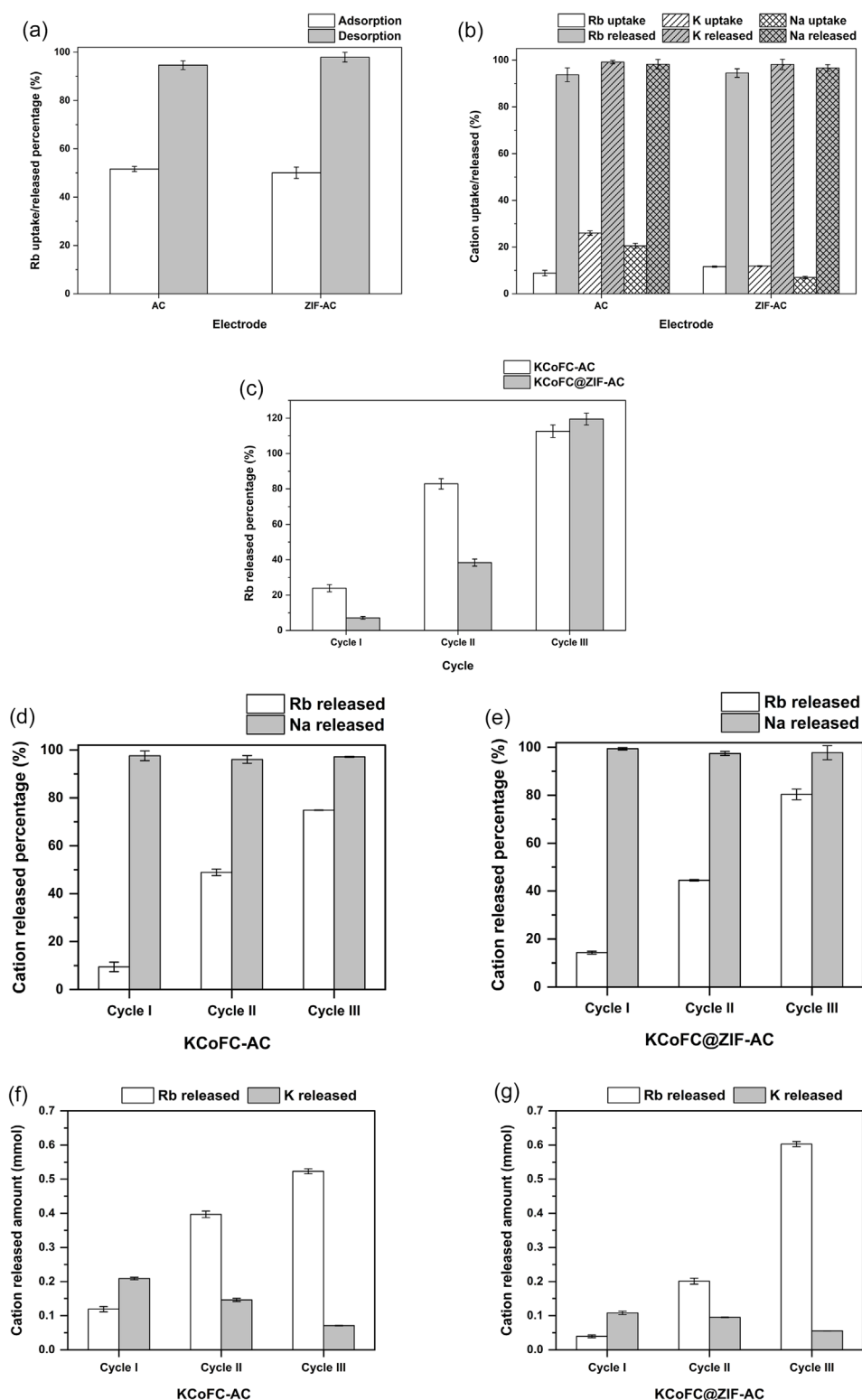
2500273 (7 of 15)

Figure 5. a,b) Comparison between the AC and ZIF-AC electrodes regarding cation adsorption and desorption rates in Rb single and mixed monovalent solutions; c) comparison of Rb released (%) between KCoFC-AC and KCoFC@ZIF-AC electrodes during desorption phase with Rb single solution for three consecutive cycles; d,e) comparison between KCoFC-AC and KCoFC@ZIF-AC electrodes regarding cation released percentage (%) during the desorption phase in the test with mixed monovalent solution for three consecutive cycles (Due to the minus value of the K uptake percentage (%) by the KCoFC-AC and KCoFC@ZIF-AC electrodes in the adsorption phase, the K released percentage is not calculated and presented); and f,g) amount of Rb and K released (mmol) during desorption phase from KCoFC-AC and KCoFC@ZIF-AC electrodes with Rb single solution for three consecutive cycles.

attraction.[57] It results in a weak ion binding strength between the cations and the carbonaceous layer; thus, facile nonselective ion liberation occurs by applying the reversed voltage condition.[48,57] To further support this argument, previous studies have reported that the presence of additional mechanisms—such as chemisorption—within carbon-based electrodes can lead to a decrease in their desorption efficiency.[58–62] In such cases, the strong chemical interactions between the ionic species and the functional groups on the electrode surface result in enhanced binding affinity, thereby hindering the ion release process. For instance, Cuong et al.[62] introduced a layered double hydroxide induced activated carbon electrode (MAAC) in a membrane CDI configuration for the phosphorus (P) recovery. During the discharge phase, the reduction in P release efficiency is attributed to the robust interaction between the P ions in the aqueous solution and the functional groups on the electrode surface. Concerning the present study, when the electrode was modified by incorporating Rb-selective materials (specifically KCoFC and KCoFC@ZIF), the presence of an additional ion-exchange mechanism may lead to significant changes in the ion desorption behavior. Details about the desorption performance of the fabricated KCoFC-AC/KCoFC@ZIF-AC electrodes are discussed in the following section.

2.5.2. Rb Desorption with KCoFC-AC and KCoFC@ZIF-AC Electrodes

On the contrary, KCoFC-AC and KCoFC@ZIF-AC electrodes exhibited insignificant desorption performance in the first cycle. In particular, after the adsorption test with Rb single solution, the Rb desorption rate of KCoFC-AC and KCoFC@ZIF-AC electrodes was 24% and 7%, respectively (Figure 5c). As discussed, the ion exchange process controls the Rb uptake of the fabricated KCoFC and KCoFC@ZIF electrodes; thus, the chemisorption mechanism creates a strong bonding between the Rb species and the KCoFC crystal lattice. Therefore, in the first desorption phase, the reversed charge may not overcome the required energy barrier to release the Rb-captured ions inside the inner cavities of the KCoFC particle. Equivalently, the corresponding metrics of KCoFC-AC and KCoFC@ZIF-AC electrodes in the experiment with the mixed solution were 9% and 14%, respectively, which were negligible in comparison with the discharged percentage of Na (>97%) and K (>100%) (Figure 5d,e). This can be explained by the fact that the KCoFC-based electrodes have a low uptake preference for Na in the aqueous solution. Thus, the majority of Na ions were attracted to the external surface of KCoFC and KCoFC@ZIF nanoparticles and the macropores of the activated carbon media by the low physical binding force. Thus, these ions could be favorably detached under the effect of a reversed charge. In addition, the ion-exchange mechanism between the K substitutable group in the KCoFC lattice and Rb in the aqueous phase also contributes to the liberated portion of K ions (slightly higher than 100%).

Three cycles of adsorption–desorption sequences were conducted for KCoFC-AC and KCoFC@ZIF-AC with Rb only and mixed Rb solution (Figure 5d,e). Cycle I, showed minimal Rb desorption for both electrodes, followed by noticeably higher desorption rates in the later cycles. Conversely, Na desorption

followed a straightforward desorption (≈100%) for all three cycles. These results indicate that due to the weak physical adsorption of Na onto the outer surface of KCoFC, it was easily desorbed with reverse charge. This pattern was in line with Rb desorption with AC and ZIF-AC electrodes. Contrarily, due to the ion exchange mechanism between Rb and K in the inner pores of KCoFC, Rb was firmly attached to the internal pores of the nanomaterial. As such, the electrochemical reverse charge could not comprehensively discharge Rb ions. Upon complete ion exchange between Rb-K in three cycles, Rb is likely fully saturated onto the ion exchange material. Consequently, by cycles II and III, Rb could be released by electrochemical reverse charge. Specifically, more than 100% and around 80% of desorption in cycle III could be observed in the studies with Rb single solution and mixed solution, respectively; thus, it was established that the accumulated Rb in the inner material was effectively released.

It should also be mentioned that the Rb desorption occurred alongside the K desorption. According to Figure 5f,g, in the cyclic study with Rb single solution, the mole amount of Rb discharged into the aqueous phase increased notably after each desorption attempt. In contrast, the quantity of K liberated from both electrodes to the bulk liquid reduced gradually. This phenomenon indicates the incremental saturation of the fabricated electrodes during the long-period operation. Furthermore, the KCoFC@ZIF-AC electrode showed significantly less K desorption while achieving the same amount of Rb recovered as the KCoFC-AC electrode. This result suggests that the addition of ZIF nanomaterial into the KCoFC-AC electrode has the efficacy of preventing K portions in the crystal lattice from being discharged into the solution during the desorption stage, thus maintaining the Rb uptake capacity for the subsequent adsorption cycle.

2.6. Reusability of KCoFC-AC and KCoFC@ZIF-AC Electrodes

To explore the reusability of the fabricated electrodes (i.e., KCoFC-AC and KCoFC@ZIF-AC), a total of five electrosorption/desorption cycles were carried out.

Figure 6 demonstrates the performance of these electrodes in the Rb solution study. In the electrosorption stage, the Rb sorption percentage decreased gradually from 54.21% to 44.88% and from 56.83% to 49.73% for the KCoFC-AC and KCoFC@ZIF-AC electrodes, respectively, after five ion uptake cycles (Figure 6a,c). Furthermore, the amount of K released from the KCoFC lattice in these electrodes during the electrosorption process was also recorded. Specifically, the quantity of the departed K ions dropped noticeably from 0.148 mmol in the first cycle to ≈0.003 mmol in the last cycle of the KCoFC-AC electrode (Figure 6b). A similar pattern is also observed in the test with the KCoFC@ZIF-AC electrode when the liberated amount of potassium decreased from 0.087 to 0.013 mmol (Figure 6d). Given that the predominant Rb recovery mechanism utilizing KCoFC/KCoFC@ZIF electrodes is the ion-exchange process between the K functional group and Rb in bulk fluid, the depletion of the exchangeable potassium ions after each electrosorption cycle is relevant to a step-by-step reduction of the Rb uptake performance.
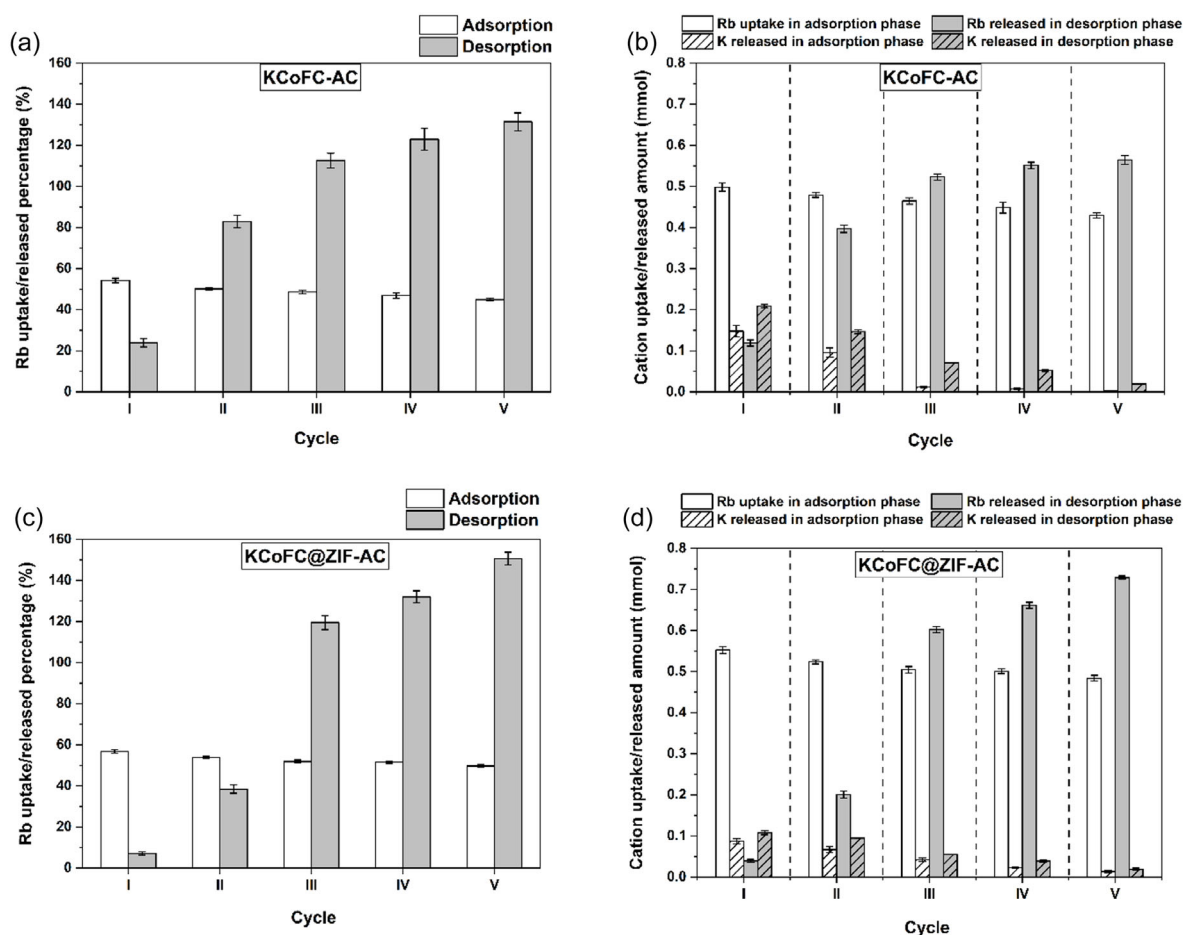
Figure 6. Multiple cyclic performances in Rb single solution study regarding a) Rb uptake/released percentage and b) amount of Rb/K uptake/released (mmol) for KCoFC-AC electrode; c) Rb uptake/released percentage and d) amount of Rb/K uptake/released (mmol) for KCoFC@ZIF-AC electrode.

In the mixed monovalent solution study utilizing the KCoFC-AC electrode (**Figure 7**a), the Rb uptake rate decreased steadily from 46.12% to 35.34% after five consecutive adsorption–desorption cycles. On the contrary, the percentage of K removal increased slightly from −0.50% to 13.24%, while the corresponding value for Na remained at around 11-12%. Consequently, the relative Rb uptake toward Na (ρ_{Na}^{Rb}) and K (ρ_{K}^{Rb}) was maintained higher than 2.68 during five cycles, indicating the high preference of the synthesized KCoFC electrode for Rb capture compared to other cations with similar valence (Figure 7b). Moreover, as can be observed from Figure 7c, although the performance of the KCoFC@ZIF-AC electrode in the mixed solution displayed a closely similar trend to the KCoFC-AC electrode, ion uptake rates were enhanced notably. In particular, the Rb uptake rate from the synthetic solution achieved 47.01% at the initial cycle, then reduced to 38.23% for the following four sequences. Conversely, the equivalent value for K increased from −3.97% to 9.20% during the entire period. Besides, the Na uptake rate remained steady at around 11%. As a result, Figure 7d demonstrates the high Rb selectivity over K ($\rho_{K}^{Rb} = 9.84$) in the fourth cycle; then, it was reduced to 4.15 by the last cycle. Furthermore, the remarkably high Rb selectivity

toward Na ($\rho_{Na}^{Rb} = 3.10$–4.36) was also observed. Interestingly, these outcomes indicate a higher Rb favourability of the ZIF-encapsulated KCoFC electrode than the pristine KCoFC electrode, which is in line with the discussion in Section 2.4.

To further assess the structural stability of the materials after multiple operation cycles, XRD analysis was conducted on the AC, KCoFC-AC, and KCoFC@ZIF-AC electrodes before and after ten consecutive adsorption–desorption cycles in the CDI system. As shown in **Figure 8**, the characteristic diffraction peaks of activated carbon, observed at 2θ values of $\approx26.4°$ and 54.5°, remained unchanged after the cycling process, indicating that the graphitic microcrystalline structure of activated carbon was preserved. For the KCoFC-AC and KCoFC@ZIF-AC composites, diffraction peaks corresponding to the cubic structure of KCoFC were detected at 2θ values of 17.6° and 35.7° (indicated by dotted lines in the figure). After five cycles, a slight shift of these peaks toward higher 2θ angles was observed, suggesting a minor lattice contraction. Importantly, no significant reduction in peak intensity was detected for any of the samples, confirming the retention of crystallinity and structural integrity throughout the CDI operation. These results collectively demonstrate the robust stability of the electrode materials under repeated cycling conditions.
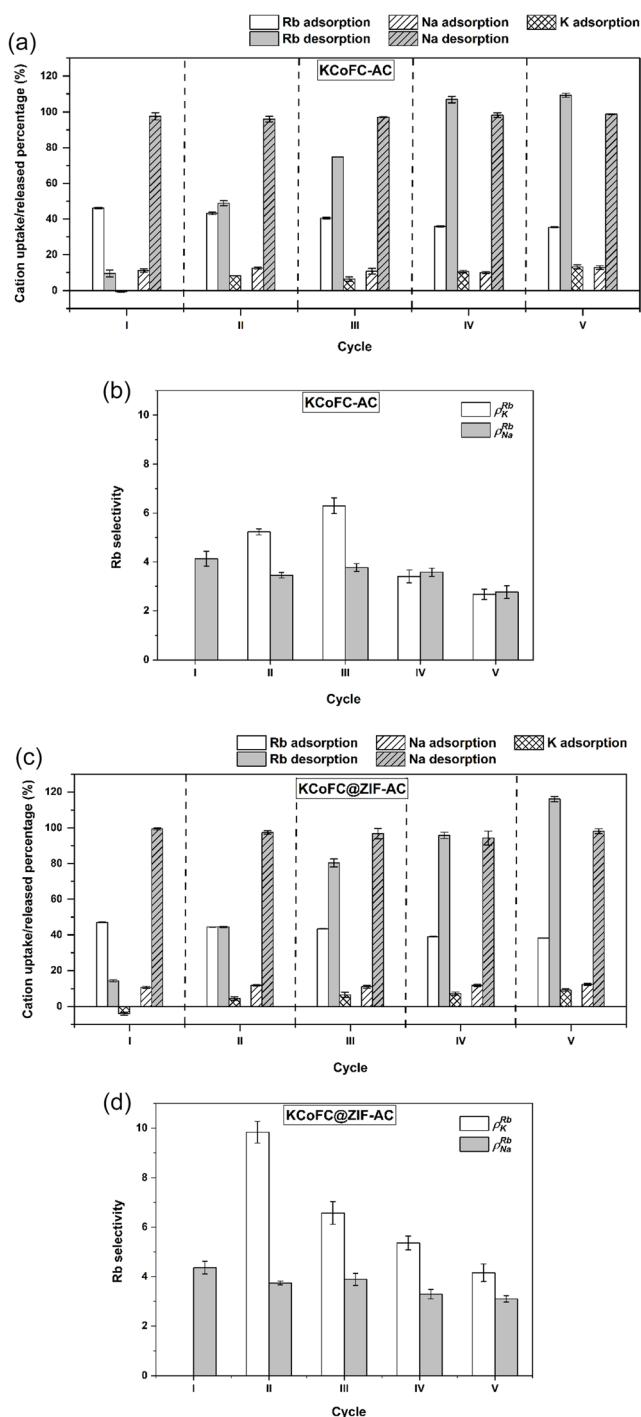
Figure 8. XRD patterns of AC, KCoFC-AC, and KCoFC@ZIF-AC electrodes before and after 10 consecutive operational cycles.

Figure 7. Multiple cyclic performances in mixed monovalent solution study regarding a) Cation uptake/released percentage and b) Rb selectivity for KCoFC-AC electrode; c) cation uptake/released percentage and d) Rb selectivity for KCoFC@ZIF-AC electrode.

According to the results, it is apparent that both electrodes can be reused for up to five cycles. However, the trend of reduced Rb uptake after each cycle indicates that a chemical regeneration may be needed to ensure that K-Rb ion exchange can be maintained. Hence, regeneration is explored in the subsequent section.
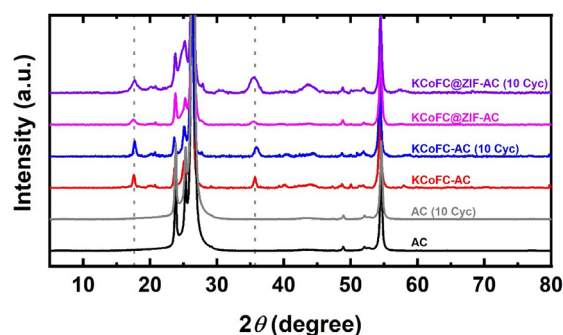
2.7. Regeneration of Saturated KCoFC-AC and KCoFC@ZIF-AC Electrodes

Chemical regeneration of the saturated electrodes was carried out with KCl solution, in line with our previous studies[8–10,12] that have established the suitability of regenerating KCoFC and KCoFC@ZIF nanomaterials with KCl due to the direct ion exchange between K-Rb.

As can be observed from **Figure 9**, KCoFC-AC and KCoFC@ZIF-AC electrodes showed similar capability to be regenerated and reused for Rb uptake. In comparing the performance of these electrodes, KCoFC@ZIF-AC exhibited a more stable trend in Rb uptake capacity, whereby, in the initial series, a slightly higher Rb uptake capacity trend was achieved. These results establish that periodic KCl regeneration is essential for both these electrodes to maintain their ion exchange capability and selective Rb capacity in repeated adsorption/desorption series.

2.8. Performance of Fabricated Electrodes with Actual Seawater Solution

The selective Rb performance capability of the fabricated electrodes was evaluated with actual seawater and Rb-spiked seawater solutions.

In the presence of major cations in seawater with significantly higher concentration ratios to Rb (Ca/Rb = 75/1, K/Rb = 78/1, Mg/Rb = 253/1, and Na/Rb = 2114/1, respectively), both electrodes showed an extraordinary selective Rb uptake rate (≈90%), with minimal uptake of all other major cations (**Figure 10**). It is worth highlighting that while KCoFC@ZIF-AC electrode exhibited a similar Rb uptake capacity to KCoFC@AC electrode, the uptake of all other major cations in seawater (Na, K, Ca, and Mg) was significantly lower for KCoFC@ZIF-AC in both unspiked and spiked seawater samples. As a result, KCoFC@ZIF-AC achieved higher Rb selectivity. This result is attributed to the higher Rb selectivity of KCoFC@ZIF nanomaterial compared to KCoFC in seawater, as established in our previous work,[12] and aligns well with the results of the electrosorption study using a mixed monovalent solution in Section 2.4. The influence of organic constituents in seawater on Rb selectivity was not explicitly evaluated in the present work.
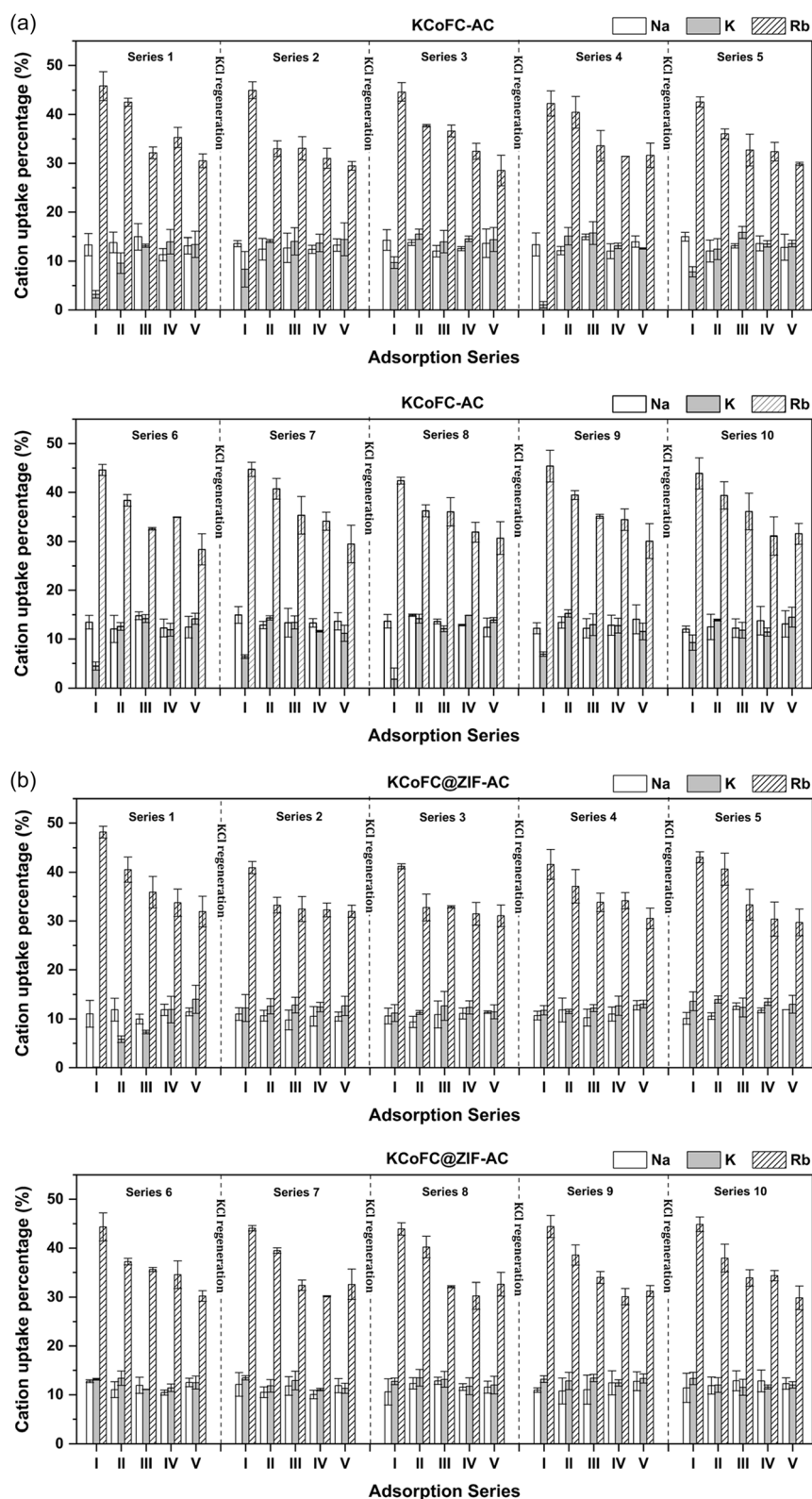
Figure 9. Cation uptake percentage of a) KCoFC-AC electrode and b) KCoFC@ZIF-AC electrode in the adsorption phase after periodic regeneration steps using 0.1 M KCl.
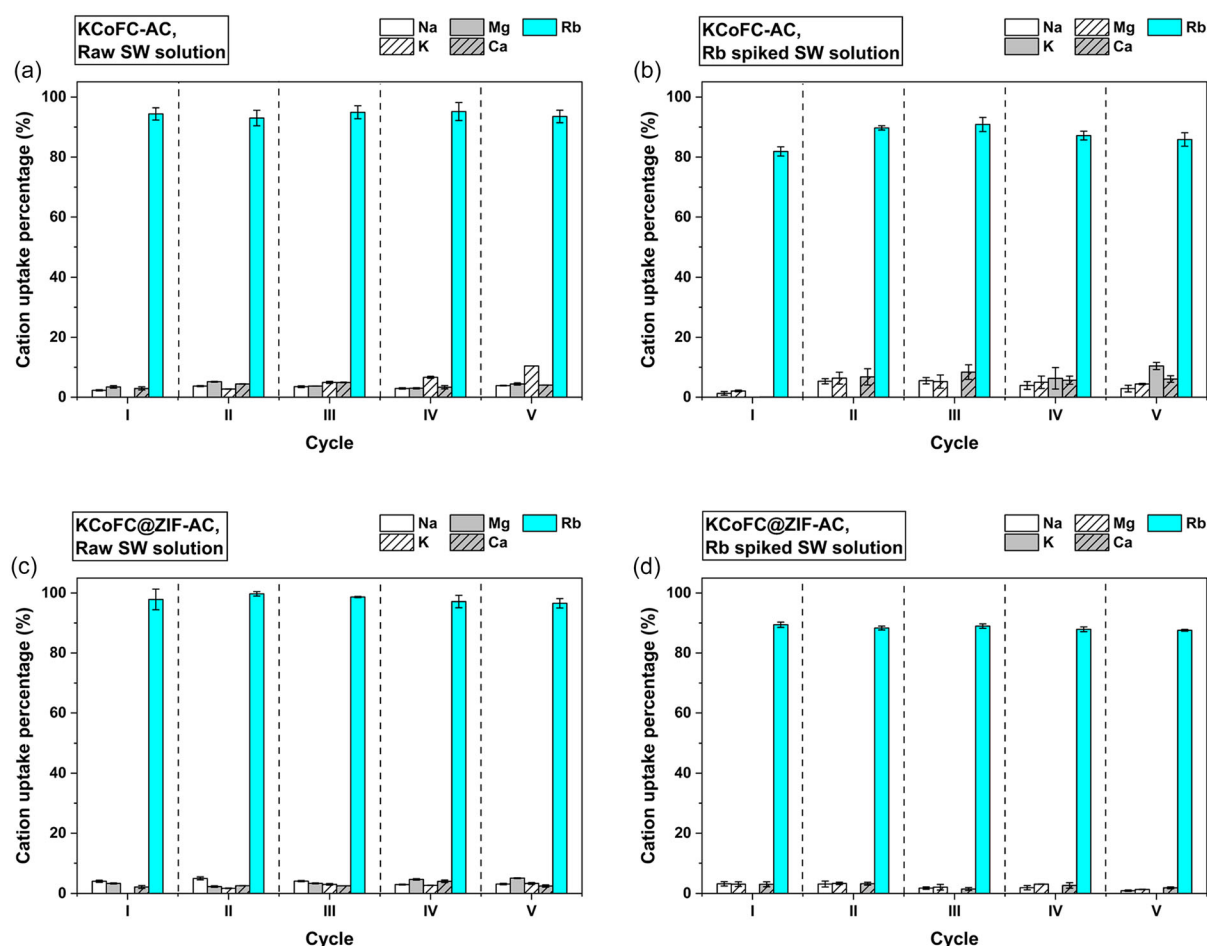
Figure 10. Cation uptake percentage of KCoFC-AC electrode in a) raw seawater solution and b) Rb-spiked seawater solution after five sorption cycles. Cation uptake percentage of KCoFC@ZIF-AC electrode in c) raw seawater solution and d) Rb-spiked seawater solution after five sorption cycles.

In our previous study,[8] we observed that organic compounds present in seawater had a negligible effect on the sorption behavior of K(M)FC for Rb recovery.

Overall, the results indicate the high capacity of the fabricated electrodes derived from KCoFC and KCoFC@ZIF nanomaterials for selectively extracting from seawater.

3. Conclusion

This work evaluated selective Rb recovery of fabricated KCoFC-AC and KCoFC@ZIF-AC nanomaterials with powdered activated carbon (AC) electrodes in CDI. Based on the results, it is highlighted: 1) The successful incorporation between KCoFC/KCoFC@ZIF ion-exchange nanomaterial and activated carbon onto the surface of the graphite layer was confirmed by several characterization analyses, including SEM, EDS, XRD, FTIR, and surface area and pore size. 2) CV and GCD measurements were carried out to evaluate the electrochemical characterization of the electrodes. The results indicated that the utilization of Rb selective nanomaterials (i.e., KCoFC/KCoFC@ZIF) sacrificed the electrodes' electric conductivities.

Thus, incorporating the conductive activated carbon component in the fabricated electrodes is necessary to maintain the charge transfer efficiency and enhance the electrosorption process. 3) Rb uptake efficiency and selectivity were enhanced significantly with KCoFC-AC and KCoFC@ZIF-AC compared to AC electrodes. The ρ_{Na}^{Rb} and ρ_{K}^{Rb} ranges for KCoFC-AC electrode were 2.77–4.13 and 2.68–5.23, respectively, whereas the KCoFC@ZIF-AC electrode presented a better Rb selectivity for both Na ($\rho_{Na}^{Rb} = 3.10$–4.35) and K ($\rho_{K}^{Rb} = 4.15$–9.84). The selectivity capacity of the fabricated electrodes is attributed to the selective ion exchange mechanism. KCoFC particles play an important role as the core material in the modified electrodes, contributing to the accessible potassium groups that can be selectively exchanged with the specific Rb cations in the aqueous solution. In addition, the ZIF nanomaterial acts as a catalyst, providing a porous and large surface area and supporting the Rb penetration pathway from the bulk phase into the KCoFC lattice. 4) Rb desorption in the composite KCoFC-AC/KCoFC@ZIF-AC electrodes occurred upon several adsorption–desorption cycles, indicating that desorption occurred only upon full saturation of the electrode due to the ion exchange mechanism. 5) Saturated electrodes demonstrated the feasibility of being reutilized several

times through periodic chemical regeneration with KCl solution, which restored the ion exchange properties of the nanomaterial. 6) Both fabricated electrodes demonstrated an outstanding Rb uptake rate ($\approx$90%) in the test with an actual seawater solution. In contrast, the ion sorption efficiencies of the other dominant cations in seawater were negligible. 7) This study provides valuable insight into the potential of KCoFC and KCoFC@ZIF as suitable materials for fabricating highly selective electrodes for rapid Rb extraction from seawater using CDI.

4. Experimental Section

Materials and Chemicals: The preparation of ZIF, KCoFC, and KCoFC@ZIF nanomaterials is described in detail in the Supporting Information.

Preparation of CDI Electrodes: The CDI electrodes were fabricated according to the procedure reported by Zhao et al.[16] Initially, 1.0 g of polyvinylidene fluoride (PVDF, Merck Chemical Co.) was dissolved in 20 mL of dimethylformamide (DMF, Merck Chemical Co.), and the mixture was stirred overnight at room temperature to achieve a uniform, high-viscosity solution. After that, the PVDF solution was poured into a beaker containing 5.0 g of activated carbon (AC, Merck Chemical Co.) and 2.5 g of KCoFC or KCoFC@ZIF adsorbent. In the next step, the mixture was vigorously mixed to form a homogeneous slurry. Thereafter, the mixture was sonicated for 1 h to prevent the formation of aggregates. Subsequently, the slurry was transferred to a film applicator, and a casting blade (thickness = 500 μm) was employed to laminate the slurry mixture onto a graphite current collector (200 $\times$ 100 mm). The composite electrodes were then left to dry overnight at 60 °C to evaporate any remaining solvent. For comparison, an electrode coated with ZIF was prepared as a control following a similar procedure described above to explore the role of ZIF on the Rb uptake.

The composite electrodes prepared using neat AC, ZIF-coated AC, KCoFC-coated AC, and KCoFC@ZIF-coated AC were denoted as AC, ZIF-AC, KCoFC-AC, and KCoFC@ZIF-AC electrodes, respectively. Figure S1, Supporting Information, illustrates a representative synthesis procedure for the KCoFC@ZIF-AC composite electrode.

Characterization: The characterization analyzes of the fabricated electrodes, including SEM, EDS, XRD, FTIR, and N_2 adsorption/desorption measurement, are summarized in the Supporting Information.

CDI Configuration: The configuration of the CDI experimental system is demonstrated in the Supporting Information. Besides, the schematic diagram of the CDI experiment and the configuration of the CDI electrochemical cell are depicted in Figure S2, Supporting Information.

CDI Experiments: Details about the electrochemical measurement and the electrosorption test using the fabricated electrodes are provided in the Supporting Information.

Supporting Information

Supporting Information is available from the Wiley Online Library or from the author.

Acknowledgements

Conflict of Interest

The authors declare no conflict of interest.

Author Contributions

Dai Quyet Truong: writing—original draft, methodology, investigation, data curation, formal analysis, visualization. **Youngwoo Choo**: methodology, validation, formal analysis, writing—review and editing, visualization. **Tien Vinh Nguyen**: supervision, writing—review and editing. **Gayathri Naidu**: conceptualization, methodology, writing—review and editing, supervision.

Data Availability Statement

The data that support the findings of this study are available from the corresponding author upon reasonable request.

Keywords

[1] U. S. G. Survey, *Mineral commodity summaries 2023*, Mineral Commodity Summaries, Reston, VA **2023**, p. 210.

[2] S. K. Sharma, D. Q. Truong, J. Guo, A. K. An, G. Naidu, B. J. Deka, *Desalination* **2023**, *556*, 116578.

[3] S. Templier, P. Cheiney, Q. d'Armagnac de Castanet, B. Gouraud, H. Porte, F. Napolitano, P. Bouyer, B. Battelier, B. Barrett, *Sci. Adv.* **2023**, *8*, eadd3854.

[4] C. V. Sulham, G. P. Perram, M. P. Wilkinson, D. A. Hostutler, *Opt. Commun.* **2010**, *283*, 4328.

[5] N. Aslam, H. Zhou, E. K. Urbach, M. J. Turner, R. L. Walsworth, M. D. Lukin, H. Park, *Rev. Phys.* **2023**, *5*, 157.

[6] P. Loganathan, G. Naidu, S. Vigneswaran, *Environ. Sci.: Water Res. Technol.* **2017**, *3*, 37.

[7] A. Kumar, G. Naidu, H. Fukuda, F. Du, S. Vigneswaran, E. Drioli, J. H. V. Lienhard, *ACS Sustainable Chem. Eng.* **2021**, *9*, 7704.

[8] G. Naidu, S. Jeong, M. A. H. Johir, A. G. Fane, J. Kandasamy, S. Vigneswaran, *Water Res.* **2017**, *123*, 321.

[9] G. Naidu, P. Loganathan, S. Jeong, M. A. H. Johir, V. H. P. To, J. Kandasamy, S. Vigneswaran, *Chem. Eng. J.* **2016**, *306*, 31.

[10] G. Naidu, T. Nur, P. Loganathan, J. Kandasamy, S. Vigneswaran, *Sep. Purif. Technol.* **2016**, *163*, 238.

[11] G. Naidu, S. Jeong, Y. Choi, M. H. Song, U. Oyunchuluun, S. Vigneswaran, *J. Clean. Prod.* **2018**, *174*, 1079.

[12] D. Quyet Truong, Y. Choo, N. Akther, S. Roobavannan, A. Norouzi, V. Gupta, M. Blumenstein, T. Vinh Nguyen, G. Naidu, *Chem. Eng. J.* **2023**, *454*, 140107.

[13] J. Kang, T. Kim, H. Shin, J. Lee, J.-I. Ha, J. Yoon, *Desalination* **2016**, *398*, 144.

[14] M. Chu, W. Tian, J. Zhao, M. Zou, Z. Lu, D. Zhang, J. Jiang, *Chemosphere* **2022**, *307*, 136024.

[15] Q. Ji, C. Hu, H. Liu, J. Qu, *Chem. Eng. J.* **2018**, *350*, 608.

[16] F. Zhao, S. Chen, H. Xiang, T. Gao, D. Wang, D. Wei, M. Sillanpää, Y. Ke, C.-J. Tang, *Carbon* **2022**, *197*, 282.

[17] Z. Qiu, Y. Li, Y. Gao, Z. Meng, Y. Sun, Y. Bai, N.-T. Suen, H.-C. Chen, Y. Pi, H. Pang, *Angew. Chem. Int. Ed.* **2023**, *62*, e202306881.

[18] H. Wang, H. You, G. Wu, L. Huang, J. Yan, X. Liu, Y. Ma, M. Wu, Y. Zeng, J. Yu, H. Zhang, *Chem. Eng. J.* **2023**, *460*, 141621.

[19] G. Zhang, Y. Lu, Y. Yang, H. Yang, Z. Yang, S. Wang, W. Li, Y. Sun, J. Huang, Y. Luo, H.-Y. Chen, Y.-F. Liao, H. Ishii, S. Gull, M. Shakouri, H.-G. Xue, Y. Hu, H. Pang, *J. Am. Chem. Soc.* **2024**, *146*, 16659.

[20] M. Rethinasabapathy, G. Bhaskaran, S.-K. Hwang, T. Ryu, Y. S. Huh, *Chemosphere* **2023**, *336*, 139256.

[21] B. Hu, B. Zhang, Y. Wang, M. Li, J. Yang, J. Liu, *Desalination* **2023**, *560*, 116662.

[22] A. Siekierka, M. Bryjak, *Desalination* **2021**, *520*, 115324.

[23] X. Shang, B. Hu, P. Nie, W. Shi, T. Hussain, J. Liu, *Sep. Purif. Technol.* **2021**, *258*, 118009.

[24] S. Roobavannan, Y. Choo, D. Q. Truong, H. K. Shon, G. Naidu, *Chem. Eng. J.* **2024**, *483*, 149242.

[25] S. Roobavannan, Y. Choo, D. Q. Truong, D. S. Han, H. K. Shon, G. Naidu, *Chem. Eng. J.* **2023**, *474*, 145957.

[26] S. Wang, H. Zhuang, X. Shen, L. Zhao, Z. Pan, L. Liu, S. Lv, G. Wang, *J. Hazard Mater.* **2023**, *457*, 131785.

[27] S.-H. Lee, M. Choi, J.-K. Moon, S.-W. Kim, S. Lee, I. Ryu, J. Choi, S. Kim, *Colloids and Surf. A* **2022**, *647*, 129175.

[28] E. Q. Kaadhm, K. D. Salman, A. H. Reja, *J. Phys.: Conf. Ser.* **2021**, *1973*, 012052.

[29] B. Cahyono, Q. A'yun, M. Suzery, *IOP Conf. Ser.: Mater. Sci. Eng.* **2018**, *349*, 012010.

[30] A. Hanif, H. N. Bhatti, M. A. Hanif, *Ecol. Eng.* **2009**, *35*, 1427.

[31] Y. Bondar, Y. Olkhovyk, S. Kuzenko, *J. Radioanal. Nucl. Chem.* **2021**, *330*, 1221.

[32] O. Gibert, C. Valderrama, M. Peterková, J. L. Cortina, *Solvent Extr. Ion Exch.* **2010**, *28*, 543.

[33] X. Yan, Y. Li, X. Hu, R. Feng, M. Zhou, D. Han, *Chin. J. Chem. Eng.* **2021**, *33*, 279.

[34] J. Yao, R. Chen, K. Wang, H. Wang, *Microporous Mesoporous Mater.* **2013**, *165*, 200.

[35] S. M. Lee, S. H. Lee, D.-H. Jung, *J. Ind. Eng. Chem.* **2024**, *137*, 195.

[36] D. V. Cuong, P.-C. Wu, N.-L. Liu, C.-H. Hou, *Sep. Purif. Technol.* **2020**, *242*, 116813.

[37] M.-C. Wu, Y.-H. Kao, C.-H. Hou, *J. Environ. Chem. Eng.* **2024**, *12*, 113104.

[38] M. A. Zabara, G. Katırcı, B. Ülgüt, *J. Phys. Chem. C* **2022**, *126*, 10968.

[39] M. A. Zabara, G. Katırcı, F. E. Civan, A. Yürüm, S. A. Gürsel, B. Ülgüt, *Electrochim. Acta* **2024**, *485*, 144080.

[40] X. Zhang, H. Zhou, H. Zhang, *Environ. Sci. Technol.* **2024**, *58*, 14886.

[41] F. Sun, X. Peng, X. Bai, Z. Chen, R. Xie, B. He, P. Han, *RSC Adv.* **2022**, *12*, 16979.

[42] M. Mossad, L. Zou, *J. Hazard. Mater.* **2012**, *213*, 491.

[43] K. Z. Huang, H. L. Tang, *Environ. Technol.* **2020**, *41*, 3456.

[44] Z. Zhang, T. Zhao, Z. Zhao, L. He, W. Xu, D. Liu, W. Li, *Desalination* **2025**, *600*, 118504.

[45] Z. Zhang, T. Zhao, L. He, Z. Zhao, F. Sun, W. Xu, D. Liu, *Desalination* **2023**, *549*, 116331.

[46] X. Zeng, H. Zeng, G. Xiong, Y. Zeng, S. Zhao, H. Xiao, X. Zhang, X. Zhao, *Desalination Water Treat.* **2024**, *319*, 100533.

[47] X. Wang, X. Wang, Y. Wang, Q. Zhai, Y. Jiang, S. Li, *Sep. Purif. Technol.* **2022**, *288*, 120635.

[48] J. G. Gamaethiralalage, K. Singh, S. Sahin, J. Yoon, M. Elimelech, M. E. Suss, P. Liang, P. M. Biesheuvel, R. L. Zornitta, L. C. P. M. de Smet, *Energy Environ. Sci.* **2021**, *14*, 1095.

[49] C.-H. Hou, C.-Y. Huang, *Desalination* **2013**, *314*, 124.

[50] S. M. Hossain, H. Yu, Y. Choo, G. Naidu, D. S. Han, H. K. Shon, *Desalination* **2023**, *546*, 116201.

[51] P. Liu, T. Yan, J. Zhang, L. Shi, D. Zhang, *J. Mater. Chem. A* **2017**, *5*, 14748.

[52] J. Duan, S. Bao, Y. Zhang, *Chem. Eng. Res. Des.* **2018**, *132*, 178.

[53] S. P. Hong, H. Yoon, J. Lee, C. Kim, S. Kim, J. Lee, C. Lee, J. Yoon, *J. Colloid Interface Sci.* **2020**, *564*, 1.

[54] Y. Jiang, Z. Wan, X. He, J. Yang, *Angew. Chem. Int. Ed.* **2023**, *62*, e202307274.

[55] T. Parker, Y. Zhang, K. Shevchuk, T. Zhang, V. Khokhar, Y.-H. Kim, G. Kadagishvili, D. Bugallo, M. Tanwar, B. Davis, J. Kim, Z. Fakhraai, Y.-J. Hu, D.-E. Jiang, D. V. Talapin, Y. Gogotsi, *ACS Nano* **2025**, *19*, 22228.

[56] X.-L. Fu, F. Zheng, S.-J. Xie, Y.-L. Ji, C.-J. Gao, *Phys. Chem. Chem. Phys.* **2024**, *26*, 22220.

[57] X. Zhao, H. Wei, H. Zhao, Y. Wang, N. Tang, *J. Electroanal. Chem.* **2020**, *873*, 114416.

[58] T. Wang, H. Liang, L. Bai, X. Zhu, Z. Gan, J. Xing, G. Li, T. M. Aminabhavi, *Chem. Eng. J.* **2020**, *384*, 123277.

[59] Z. Sun, Q. Li, L. Chai, Y. Shu, Y. Wang, D. Qiu, *Chemosphere* **2019**, *229*, 341.

[60] R. Liu, Y. Sui, X. Wang, *Chem. Eng. J.* **2019**, *371*, 903.

[61] M. He, P. Zhang, X. Zhang, F. Li, S. Huo, D. Fang, B. Liang, K. Li, *J. Clean. Prod.* **2022**, *361*, 132262.

[62] D. V. Cuong, C.-H. Hou, V.-A. Nguyen, T. T. V. Nga, *J. Environ. Chem. Eng.* **2024**, *12*, 113676.